The Motion of Simulated Convective Storms as a Function of Basic Environmental Parameters

J. CODY KIRKPATRICK

University of Alabama in Huntsville, Huntsville, Alabama

EUGENE W. MCCAUL JR. AND CHARLES COHEN

Universities Space Research Association, Huntsville, Alabama

(Manuscript received 2 February 2006, in final form 30 November 2006)

ABSTRACT

Based on results from a three-dimensional cloud-resolving model, it is shown that simulated convective storm motions are affected by thermodynamic as well as kinematic properties of the environment. In addition to the mean wind and its vertical shear, the effect on isolated storm motion of parameters such as bulk convective available potential energy (CAPE), the vertical distribution of buoyancy in the profile, the heights of the lifting condensation level (LCL) and level of free convection (LFC), and cloud-base temperature is considered. Storm motions show at least some sensitivity to all input parameters. Consistent with previous studies, hodograph radius has the most pronounced effect, but the vertical distribution of shear (which also influences the mean wind) affects storm evolution and propagation, even when the effective hodograph radius is unchanged. Among the thermodynamic parameters, the most significant variations occur when the LCL–LFC configuration is modified or when cloud-base temperature is changed. The effects of increases in bulk CAPE act mainly to increase the temporal variability of storm motions. This temporal variability is found to consist both of oscillations about a mean state and trends (accelerations) and is related to increases in the complexity of storm evolution with increasing CAPE. The results point to the importance of environmental factors that enhance storm intensity and rotation, which play a key role in determining storm deviate motion.

1. Introduction

The motion of a convective storm is one of its most readily observed characteristics. Other common descriptors such as updraft velocity or vertical vorticity require more complex observations and calculations (e.g., retrieval techniques such as in Shapiro et al. 2003). Driven partly by features of the ambient atmospheric profile, storm motion is intimately related to the intensity of the updraft and the rotation (if present) within a storm. Cotton and Anthes (1989, p. 497) list three mechanisms to explain storm movement: (i) translation or advection by a representative mean wind; (ii) forced propagation as a result of mechanisms generally larger in scale than the convective storm (and not considered in this work); and (iii) "autopropagation," or intrastorm mechanisms such as downdraft or updraft forcing or vertical pressure perturbations. These mechanisms are not necessarily independent of one another, and many convective storms can be affected by all three mechanisms at some point in their life cycle [e.g., see Zeitler and Bunkers (2005) for additional discussion of propagation mechanisms]. The movement may also be divided into discrete (for multicell storms) or continuous propagation (for supercells). There are two modes of continuous propagation: nonlinear (which is dominant when the hodograph is nearly straight) and linear (which is significant in circular shear).

Our understanding of storm propagation has evolved considerably over the last few decades. Early observational studies of storms (e.g., Brooks 1946; Byers and Braham 1949) concluded that storm motion was best represented by the ambient winds at a particular atmospheric "steering" level. A class of convective storms

Corresponding author address: Eugene W. McCaul Jr., Universities Space Research Association, 320 Sparkman Dr., Huntsville, AL 35805.
E-mail: emccaul@usra.edu

DOI: 10.1175/MWR3447.1

known as supercells was later identified to have motions that deviate to the right (or left) of the mean wind (Browning 1962, 1964), and Marwitz (1972a,b) observed varying storm motions during the life cycle of severe hailstorms. The effects on storm propagation of updraft regeneration along a flanking line were noted by Lemon (1976). Storm motion and evolution are also affected by mesoscale boundaries (e.g., Weaver and Nelson 1982; Markowski et al. 1998) and terrain (e.g., Akaeda et al. 1995; Landel et al. 1999). The strength of the storm-induced low-level cold pool has also been shown to affect propagation in mesoscale convective systems (e.g., Corfidi 2003; Wilson and Roberts 2006), which can initiate as supercells. Presumably, the strength and depth of the cold pool can also affect the propagation of supercell updrafts (Davies-Jones 2002).

a. Theories of storm propagation

Discrete, isolated convective storms often move with nearly constant speed and direction, with small variations during the storm life cycle. After Browning's (1964) realization that certain storms did not simply follow the wind at any particular level, numerical models were employed to diagnose what additional forces were influencing storm motion. Marroquin and Raymond (1982) presented a linearized model of convective overturning to explain storm propagation; their model performed well for "weak" thunderstorms but poorly for supercells. Experiments by Wilhelmson and Klemp (1978) showed that a unidirectional shear can cause storm splitting, producing updrafts that propagate rightward and leftward off the hodograph, but failed to explain the physical mechanisms by which this deviate motion occurred.

The hydrodynamic pressure field that is induced by the intrusion of an updraft into environmental shear can affect storm propagation. The vertical gradient of this perturbation pressure has been shown to promote updraft propagation across the mean wind shear (e.g., Rotunno and Klemp 1982). The diagnostic pressure equation can take the following form [Davies-Jones 2002, his Eq. (3.3c)]:

$$-\nabla^2 p_{\rm nh} \equiv \underbrace{g\nabla_H^2 \mathfrak{M}}_{F_M} + \underbrace{2\rho_s \mathbf{S}_0 \cdot \boldsymbol{\nabla}_H w'}_{F_L} + \underbrace{\rho_s(e'_{ij}e'_{ij} - w^2\partial_{zz}\ln\rho_s)}_{F''_{\rm SPLAT}} - \underbrace{\rho_s \boldsymbol{\omega}' \cdot \boldsymbol{\omega}'/2}_{F''_{\rm SPIN}}, \quad (1)$$

where $\nabla^2 p_{\rm nh}$ is the nonhydrostatic perturbation pressure, $\mathfrak{M}$ is the column mass (that includes liquid water and ice), ρ_s is the base-state density, $\mathbf{S}_0 \equiv d_z \mathbf{v}_0$ is the environmental shear, $e'_{ij} \equiv (\partial v'_i/\partial x_j + \partial v'_j/\partial x_i)/2$ is the deviation rate-of-deformation tensor, $\boldsymbol{\omega}' \equiv \boldsymbol{\nabla} \times \mathbf{v}'$ is the deviation relative vorticity, the linear forcing is $F_{\rm LN} = F_M + F_L$, and the nonlinear forcing $F_{\rm NL}$ comprises nonlinear splat and spin forcing $F''_{\rm SPLAT}$ and $F''_{\rm SPIN}$. The nonlinear effects dominate in straight-hodograph environments, whereas linear forcing (i.e., from the ambient wind shear) dominates in environments with highly curved hodographs (Davies-Jones 2002).

The relationship between storm rotation and propagation has been well documented (e.g., Rotunno and Klemp 1982, 1985). Rotunno and Klemp showed that storm motion is a sum of the effects associated with mean flow steering and additional deviations associated with storm rotation. Weisman and Rotunno (2000) followed this hypothesis, contending that a supercell's deviant propagation is the result of its dynamically forced, rotating updraft. An alternate view (e.g., Davies-Jones 1984) asserted that updrafts will rotate cyclonically as a whole, given propagation off the hodograph and to the right of the shear vector. What is important here is that propagation across the ambient shear (i.e., deviant motion off the hodograph and to the left or right of the mean shear) and storm rotation are intimately related.

Using Petterssen's formula and the vertical equation of motion, Davies-Jones (2002) derived a nonlinear formula for updraft motion as a function of height, consisting of linear shear-induced, weight-induced (e.g., effects of water loading or cold pools), and nonlinear dynamical parts. Davies-Jones showed that linear supercell propagation off the hodograph increases with updraft width; the propagation is maintained by the nonhydrostatic vertical pressure gradient force (Newton and Newton 1959; Rotunno and Klemp 1982, 1985). The propagation is dominated by the linear shear-induced part when the hodograph is highly curved, and by the nonlinear dynamical parts in straight-hodograph environments.

b. Supercell motion forecasting

Various methods have been developed to forecast storm and supercell motion. A postulated balance of updraft and downdraft mass flux was used by Colquhoun (1980) to estimate severe thunderstorm motion. Maddox (1976) examined tornado proximity soundings to develop a mean wind profile applicable to supercells, and then estimated the motion of a cyclonically rotating supercell by adding 30° to the right of a mean wind vector (calculated using mandatory pressure levels) at 75% of the speed. Using the 0–6-km mean wind layer, Davies and Johns (1993) proposed an adjustment—20° to the right, at 85% of the speed—for supercells embedded in very strong flow (i.e., a cloud layer mean wind greater than 15 m s^{-1}). Rasmussen and Blanchard

(1998) then developed a method based on a prescribed deviation from a specified point on the mean shear vector between the lowest 0.5 km and the lowest 4 km of the atmosphere. None of these investigations, however, managed to parameterize the deviation of the storm motion from the mean shear as a function of the strength of the shear, or of any other environmental variable.

More recently, Bunkers et al. (2000, hereafter B00) proposed a method whereby supercell motion is assumed to be described by the sum of an advective component and a propagation component that arises due to the interaction of the updraft with the vertically sheared environment. Using a set of supercell soundings and observations, B00 characterized the magnitude of deviate motion from the (typically 0–6 km) mean wind using a constant parameter, D, having value 7.5 m s^{-1}. Their "internal dynamics" method produces lower mean absolute errors (MAE; 4.1 m s^{-1}) than any of the aforementioned methods. Ramsay and Doswell (2005) have revised B00, suggesting the mean wind layer be extended to 0–8 km. While the utility of these techniques—especially the widely accepted B00—is recognized, and the properties of the wind profile generally dominate the forcing of storm motion, these methods do not incorporate the possible impact of thermodynamic parameters on storm motion.

c. *Effects of thermodynamic parameters on storms*

While the refereed literature has focused almost exclusively on using the ambient wind profile to predict convective storm motion, recent modeling studies suggest that variations in the thermodynamic profile also need to be considered. "Significant modulation" of storm morphology and intensity can occur by changing only the shapes of the profiles of buoyancy and shear, either alone or in combination (McCaul and Weisman 2001, hereafter MW01). Changes to the lifting condensation level (LCL) and level of free convection (LFC) heights, as in McCaul and Cohen (2002, hereafter MC02), can also cause notable changes in storm structure, intensity, and evolution. The balance between midtropospheric storm-relative winds, storm-relative environmental helicity (SRH), and low-level absolute humidity is important for sustaining "long-lived" supercells (Brooks et al. 1994). Midtropospheric humidity can significantly affect simulated storm morphology (Gilmore and Wicker 1998), having implications for storm motions. The results presented in MW01 and MC02 highlight the need to consider additional atmospheric variables, beyond simple measures of bulk CAPE and vertical wind shear, to fully explain the evolution of discrete, isolated convective storms. The Convection Morphology Parameter Space Study (COMPASS; see MC02 and also McCaul et al. 2005, hereafter MCK05) was conceived for this purpose.

TABLE 1. Basic environmental parameters used in this study.

Parameter	Value(s)
Bulk integrated pseudoadiabatic CAPE	800, 2000, and 3200 J kg^{-1}
Radius of semicircular hodograph	8, 12, and 16 m s^{-1}
Shape of buoyancy profile	(See Fig. 1)
Shape of shear profile	(See Fig. 2)
Height of the LCL	0.5 and 1.6 km
Height of the LFC	0.5 and 1.6 km
Cloud-base temperature	15.5° and 23.5°C for LCL = 0.5 km, and 10.1° and 18.8°C for LCL = 1.6 km
Mean free tropospheric relative humidity	Fixed, 90%

2. Model and experiment design

We construct the environmental profiles for this study using the methodology of MCK05. Eight variables define the COMPASS parameter space (Table 1); the eight are chosen to represent the number of decisions required to construct an idealized atmospheric profile.

An amplitude parameter and a shape parameter define each buoyancy and shear profile. Buoyancy is defined relative to parcels that are assumed to ascend along a pseudoadiabat, where equivalent potential temperature (θ_e) is held constant using Eq. (43) of Bolton (1980). The buoyancy profile (Fig. 1), is defined by the following equation:

$$B(z') = E\left(\frac{m}{H}\right)^2 z' \exp\left(-\frac{m}{H} z'\right), \tag{2}$$

where the bulk CAPE is represented by E, the profile compression parameter is m, the tropopause-scale height is $H = 14.5$ km, and z' represents the altitude above the LFC. The value of B in Eq. (2) is proportional to the difference between the virtual potential temperatures of the environment and the assumed parcel curve on a sounding, since buoyancy can be expressed as $B = g(\theta'_v/\theta_{v_0})$, where θ'_v denotes the perturbation in virtual potential temperature from a reference state (θ_{v_0}) if only thermal buoyancy is considered. The semicircular-hodograph wind profiles (Fig. 2) are constructed in an analogous fashion, with the wind components given by

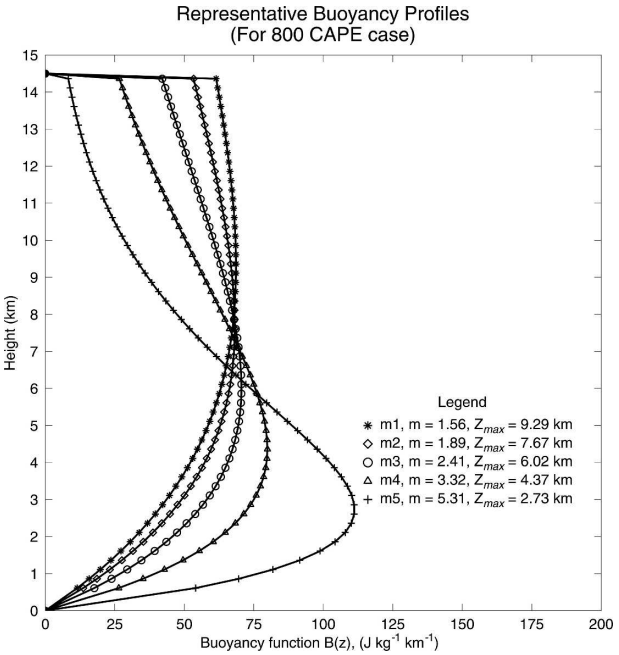

FIG. 1. Buoyancy profiles used in this study, with height above the LFC as the ordinate and the buoyancy function B as the abscissa [Eq. (2)]. The shape parameter in our experiments is denoted as m and $Z_{\max}$ is the level of maximum buoyancy. The buoyancy profile is truncated at the tropopause ($z = 14.5$ km).

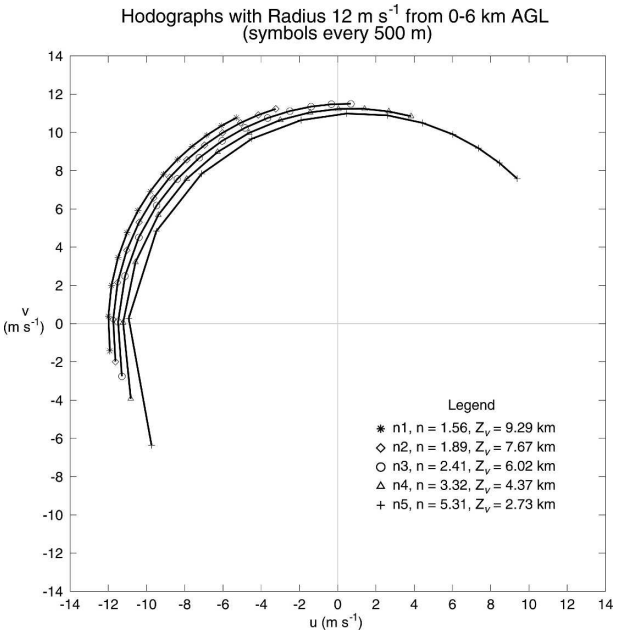

FIG. 2. Sample of hodographs and shear profiles used in this study, with symbols every 500 m. Actual hodographs extend to the tropopause but are shown here from 0 to 6 km above ground level. The shape parameter is denoted as n and Z_v is the level of maximum v wind. Curves are slightly displaced to avoid overlap; all those shown have radii of 12 m s^{-1}.

$$v(z') = c(n)V\left(\frac{n}{H}\right)^2 z' \exp\left(-\frac{n}{H}z'\right) \quad \text{and} \qquad (3)$$

$$u(z') = \text{sgn}(z' - Z_v)\sqrt{V^2 - [v(z')]^2}, \qquad (4)$$

where n is the profile compression parameter, V is the radius of the curved hodograph, and Z_v is the altitude of maximum v wind. The factor $c(n) = n^{-1}\exp(1)$ is required to ensure each v profile reaches a maximum value of V for any choice of n, and the sgn factor determines the sign that is applied to the square root. See MW01 for a more complete discussion of (2)–(4). Each shape parameter value corresponds to a function maximum at a particular altitude above the LFC for buoyancy, or above 0.5 km for the v wind.

The shape parameters for buoyancy (m) and shear (n) are discussed herein using the expressions "distributed" and "concentrated," because two different configurations are used for each value of bulk CAPE (Table 2). The distributed profile is one in which the variable (shear or buoyancy) is spread over a deeper layer with a maximum in the midtroposphere; in the concentrated profile, the level of the variable maximum is in the lower troposphere. Furthermore, distributed shear profiles have a smaller magnitude of low-level shear when compared to the concentrated shear profiles (Table 3). Note that the range of allowable shape parameters depends on the bulk CAPE. As an illustration, consider that for a very large CAPE, any attempt to specify a very low altitude of maximum buoyancy would require a low-level lapse rate greater than dry adiabatic. This is physically unrealistic. Thus, some of the more concentrated buoyancy profiles are CAPE specific, and cannot be implemented for large CAPE values.

The LCL and LFC are assigned three configurations: 0.5 and 0.5, 0.5 and 1.6, and 1.6 and 1.6 km, respectively.[1] The subcloud layer beneath the LCL is assigned a stable lapse rate to suppress turbulence, and is associated with convective inhibition on the order of 30 J kg^{-1}. The subcloud layer is a layer that features constant θ_e and constant $\partial\theta/\partial z$. All experiments have the same subcloud $\partial\theta/\partial z$, selected so as to ensure that environments do not mix out even in the lowest Richardson number cases. For the cases with a low (0.5 km) LCL and high (1.6 km) LFC, the intermediate layer is a neutral layer with a moist adiabatic lapse rate and 0.5°C dewpoint depression.

[1] The LCL actually describes mixed layer depth, and the LFC describes moist layer depth (see MC02, p. 1723).

TABLE 2. Buoyancy and shear profile shape parameters used for each value of bulk CAPE. The "x" implies that either the buoyancy (m) or shear (n) parameter may be distributed or concentrated.

CAPE (J kg^{-1})	Profile type	
	Distributed	Concentrated
800	x3	x5
2000	x2	x4
3200	x1	x3

TABLE 3. The 0–6-km bulk shear (m s^{-1}) for all hodograph configurations. The c parameter (c1, c2, c3) corresponds to the semicircular-hodograph radius. Examples of the n parameter for c2 are shown in Fig. 2. The number of supercells for each c–n combination is given in parentheses.

	c1 (R = 8 m s^{-1})	c2 (R = 12 m s^{-1})	c3 (R = 16 m s^{-1})
n1	9 (0)	14 (2)	19 (5)
n2	11 (0)	16 (3)	21 (8)
n3	12 (1)	18 (5)	24 (15)
n4	14 (2)	21 (8)	28 (9)
n5	16 (2)	24 (6)	32 (6)

Cloud-base temperatures are chosen such that precipitable water (PW) is roughly 30 mm (T_{LCL} = 15.5°C when LCL = 0.5 km) or 60 mm (T_{LCL} = 23.5°C). The low PW case (e.g., solid lines in Fig. 3) falls within reasonable bounds for environments commonly observed in midlatitude severe storm outbreaks. The high PW case represents a tropical environment with a warm cloud-base temperature. Note that the terms "low" and "high" are relative and are used only for comparison; a PW of 30 mm is not necessarily a low value in the real atmosphere (e.g., Bunkers et al. 2006, their Fig. 9). The relative humidity above the LFC [i.e., in the free troposphere (FTRH)] is a constant 90% at all levels of the simulations studied here. Potential implications of variations in FTRH will be discussed in section 4.

The radius of the quasi-semicircular hodograph[2] is varied between three values: 8, 12, and 16 m s^{-1}. Three CAPE regimes (800, 2000, and 3200 J kg^{-1}) are considered. The 800-CAPE value resembles the instability seen in many landfalling tropical cyclone tornado environments (e.g., McCaul 1991). The 2000-CAPE regime represents environments similar to those seen in many midlatitude severe storm outbreaks. Given the shear profiles examined herein, the 3200-CAPE environment represents a shear-starved environment in which the bulk Richardson number (BRN; Weisman and Klemp 1982) is outside the range predicted for supercells.[3] As a result of all the parameters combined (3 CAPE values, 3 hodograph radius magnitudes, 2 wind profile shapes and 2 buoyancy profile shapes per CAPE, 3 LCL-LFC configurations, and 2 PW values), 216 simulations are explored.

This study utilizes an updated version of the Regional Atmospheric Modeling System (Pielke et al. 1992; Walko et al. 1995), version 3b, with changes as described in MCK05. This nonhydrostatic cloud model solves the fully compressible equations of motion (Tripoli and Cotton 1982) using a time-splitting scheme (Klemp and Wilhelmson 1978) that treats sound wave modes separately. The model includes prognostic equations for six species of hydrometeors (rain, hail, graupel, pristine ice, snow, and aggregates) and a diagnostic equation for cloud water mixing ratio. Subgrid mixing

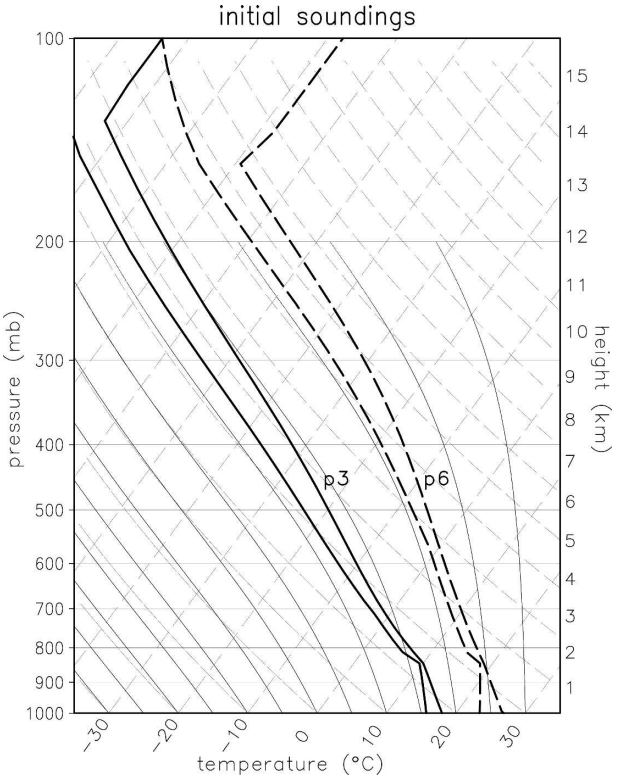

FIG. 3. Conventional skew T–log$p$ diagram with profiles illustrating the difference between a warm cloud base–high PW environment (dashed lines, labeled p6) and a cold cloud base–low PW environment (solid lines, labeled p3).

[2] Straight hodographs are being explored but are not the focus of this study.

[3] The shear profiles used herein, at 3200 CAPE, feature BRNs from 50 to 366. See Rasmussen and Blanchard (1998) for a proximity sounding-based study that discusses the relationship between BRN and observed storm type.

processes are parameterized using the deformation-based scheme of Smagorinsky (1963), with the stability modifications of Lilly (1962). Microphysical parameters that determine the size distributions of each particle species are the same in all simulations, minimizing the effects of variations in environmental microphysics on the interpretation of the results.[4]

The present work is based on the COMPASS simulation archive, which neglects the effects of topography, frontal boundaries, and other types of surface convergence (i.e., other "mesoscale forcing"; Foote 1985; Weckwerth and Parsons 2006). Each simulation is initiated with a moist, LCL-conserving thermal bubble in an otherwise horizontally homogeneous domain. The Coriolis acceleration is neglected. All simulations are carried out for 120 min, and full model history output files are saved every 5 min. Relevant numerical and physical parameter values used in our version of the model are provided in Table 4.

TABLE 4. Model numerical and physical parameters.

Parameter	Value
Horizontal domain extent	75 km × 75 km
Horizontal grid spacing	500 m
Vertical domain extent	24.5 km
Mean vertical grid spacing	500 m
Gravity wave phase velocity (for $V = 8$ and 12 m s^{-1})	15 m s^{-1}
Gravity wave phase velocity (for $V = 16$ m s^{-1})	25 m s^{-1}
Large time step	4.0 s
Acoustic time step	0.8 s
Simulation length	120 min
Coriolis parameter	0 s^{-1}

Storm motion is determined by identifying the location of the maximum updraft velocity at a model level approximately 1.9 km above the LFC, with locations noted at 5-min intervals. Only storms with updrafts of at least 2 m s^{-1} that persist for the entire 120-min simulation are analyzed. Storm motions from each 5-min interval in the simulation's second hour are then averaged to provide a best estimate of overall storm motion. This process is carried out for both the dominant right-moving (presented herein) and left-moving storms. The mean temporal standard deviation over all right-moving supercells in our simulations is 1.6 m s^{-1} (this standard deviation is actually a function of CAPE, discussed below). This sets a first threshold above which variations in storm motion can be deemed "significant" and thereby worthy of further study.

It is important to demonstrate that a model can accurately represent storm motions for a range of environmental conditions. A series of five carefully selected case studies for which plausible environmental profiles could be constructed, and for which the environments are believed to be uncontaminated from the effects of preexisting fronts or boundaries, is presented in the appendix. Despite the inherent limitations associated with subjectively modifying soundings, the model appears to reproduce observed storm motions to within 2–3 m s^{-1} in all cases. This is only slightly larger than the average temporal variability of storm motions in the COMPASS archive. Thus, we believe that our model is a suitable tool to use in studying storm motion sensitivities using numerical simulations.

Sensitivity tests involving translation of the starting hodographs confirm that the storm motions are almost entirely Galilean invariant (see discussion in B00; Rasmussen and Blanchard 1998). That is to say, within the eight-dimensional parameter space, the hodograph-relative storm motion is very nearly the same regardless of the placement of the starting hodograph. Thus, it is believed that it is safe and appropriate to try to draw conclusions about how each of the eight basic environmental parameters influences the simulated storm motions.

3. Results

Of the 216 simulations considered, 139 produced a distinct right-moving storm with a mean updraft velocity in the second hour of at least 10 m s^{-1}. We classify the storm as a supercell if it meets both of the following criteria, averaged over the simulation's second hour: (i) an updraft-vorticity correlation coefficient (see, e.g., Weisman and Klemp 1984) of 0.4 or greater; and (ii) maximum vertical vorticity (at any level) of at least 0.01 s^{-1}. This produces 72 supercell simulations; the remaining 67 are categorized as nonsupercells. The distribution of the 72 supercell cases across the parameter space (Fig. 4) is not surprising, with moderate-to-strong shears roughly balancing similar values of CAPE. This mirrors the simulations of Weisman and Klemp (1982, 1984), whose simulations produced supercells in environments with adequate CAPE (usually greater than 2000 J kg^{-1}) and shear (semicircular-hodograph radii greater than 9 m s^{-1}, or straight-hodograph lengths 30–45 m s^{-1}). Generally, the BRN distribution of our supercells is reasonable (median 37; interquartile range

[4] The distributions and mean particle sizes of hail and graupel particles can impact simulated storms (Cohen and McCaul 2006; van den Heever and Cotton 2004).

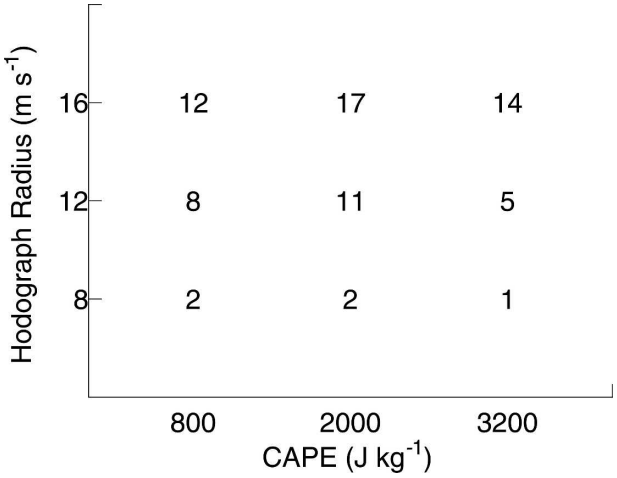

FIG. 4. Distribution of COMPASS supercells as a function of CAPE and hodograph radius. Each point in the 3 × 3 matrix represents 24 possible simulations.

19–49), but there were three supercell simulations with excessively high BRNs (greater than 150).[5]

Both supercell and nonsupercell storm motions are affected, to varying degrees, by all the parameters studied. Sensitivities are reasonably similar between the two sets, and thus supercells will be given the most attention here. Given the scarceness of supercells when the hodograph radius is only 8 m s^{-1}, these storms will be mentioned only briefly. Figures 5 and 6 present the mean mature right-moving supercell motions for the 12 and 16 m s^{-1} hodograph radius environments, respectively. Each panel in each figure describes the storm motions for one hodograph radius and shear profile shape. In other words, for all the experiments in each panel, supercell motion forecasting techniques such as B00 produce *only one forecast motion*. In this way we can identify any sensitivity of storm motion to parameters other than the hodograph.

a. Effects of shear profile radius and shape

In the mean, both supercells and nonsupercells tend to deviate farther off the hodograph when the hodograph radius is increased (Fig. 7).[6] This is evidently a response to the increased bulk shear. Unsurprisingly, the mean deviate motions for supercells are always larger than for nonsupercells, within each hodograph radius class. Storms also tend to have stronger and wider updrafts as the bulk shear is increased, as indicated by the response of the supercells to an increase in hodograph radius from 12 to 16 m s^{-1} in Fig. 8 (see also Brooks and Wilhelmson 1993). The only exceptions are the 800-CAPE cases, which have BRNs ranging from 5 to 13 when the hodograph radius is 16 m s^{-1}, and thus tend to be come severely sheared in that regime. The supercell mean second-hour updraft velocity (WMAX) response of the 3200-CAPE storms to the increase in bulk shear is particularly pronounced, apparently because those storms are somewhat shear starved when the hodograph radius is only 12 m s^{-1}.

According to theory (Davies-Jones 2002), updrafts in

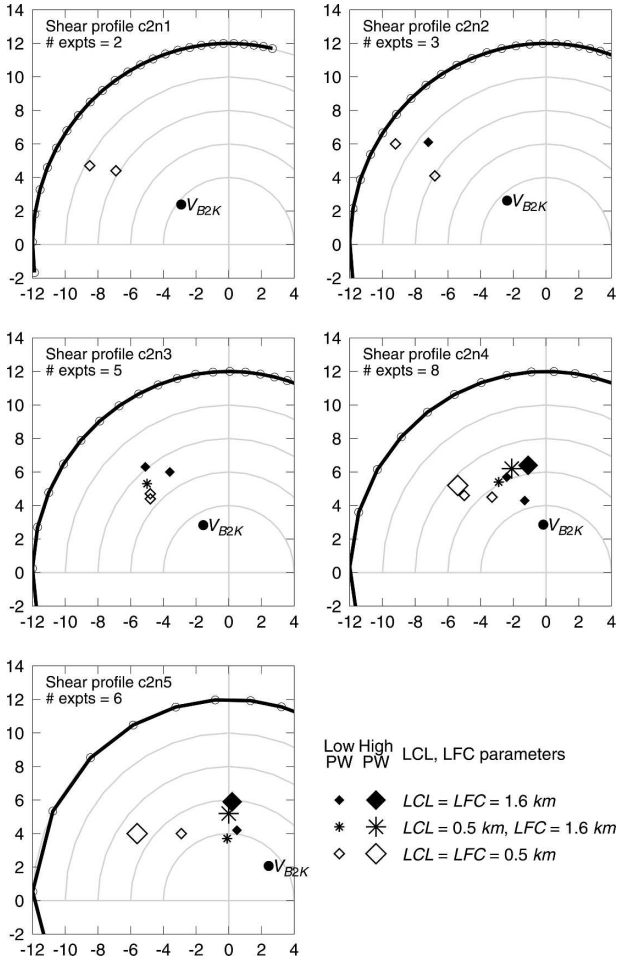

FIG. 5. Motions of supercells in simulations with $R = 12$ m s^{-1} as a function of shear profile shape, LCL and LFC heights, and PW. Effects of CAPE and the buoyancy profile are not shown. Identical symbols represent a pair of simulations with different buoyancy profile shapes. Here, V_{B2K} is the forecast storm motion using the B00 technique.

[5] All three high BRN simulations feature 3200 CAPE, a low LCL–LFC, and low PW. Hodographs (BRNs) in the three simulations are c1n3 (197), c2n1 (162), and c2n1 (162).

[6] The amount of deviate motion off the hodograph is defined as the vector magnitude of the difference between the ground-relative storm motion and the nearest point on the hodograph; this is a straightforward calculation since all our hodographs have constant radius and are centered at the origin.

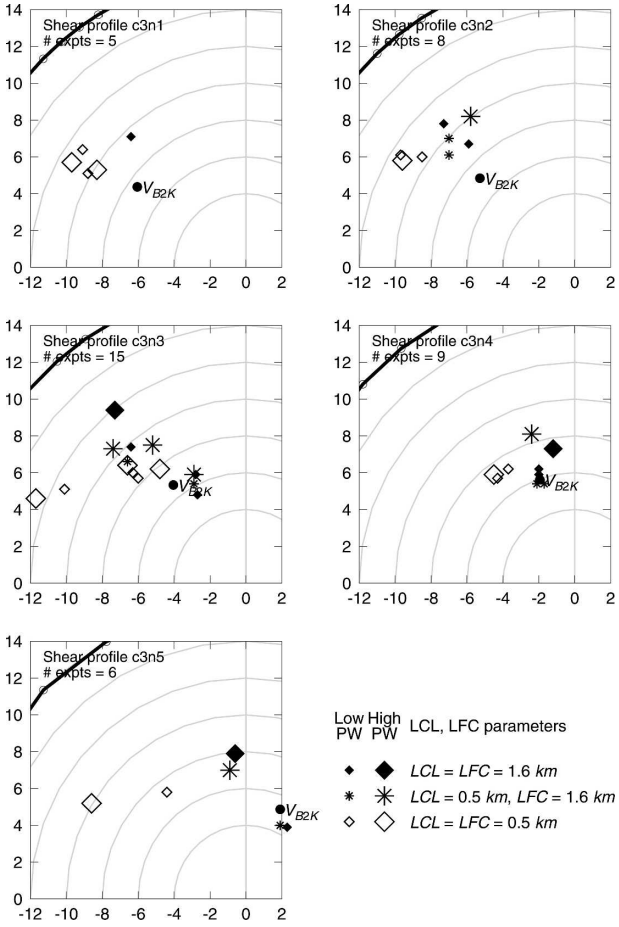

FIG. 6. Same as in Fig. 5, but for $R = 16$ m s^{-1}.

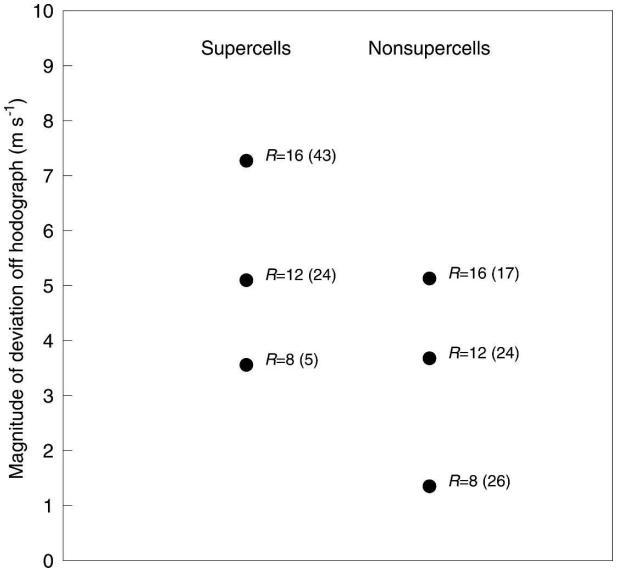

FIG. 7. Magnitude of mean storm deviation off the hodograph as a function of hodograph radius (R; m s^{-1}) for supercells and for nonsupercells. The number of simulations that compose each point is given in parentheses.

circularly curved shear that are wider and stronger will propagate linearly farther off the hodograph than narrower, weaker ones. In our simulations, the linear cross correlation between updraft area [evaluated at 5 km AGL (WAREA5)] and deviate motion (Davies-Jones 2002) is found to be strong for both supercells ($r = 0.66$) and nonsupercells ($r = 0.83$). Interestingly, for the supercells the linear correlation between deviate motion and (WAREA5)$^{1.5}$ is even stronger ($r = 0.69$).

Although the general relationships illustrated in Figs. 7–8 are compelling, the even stronger trends that exist among certain individual pairs of experiments are sometimes obscured by the use of collective statistics in those figures. For example, in Fig. 8 the severely sheared 800-CAPE, 16 m s^{-1} hodograph radius group contains several low LFC cases having narrow, weak updrafts, and the trends in WMAX and WAREA5 versus hodograph radius are unclear. The smallness and weakness of the updrafts in that regime are not surprising, in that prior research (MC02) has shown how low LFCs can lead to narrower and weaker updrafts. If, however, we consider only the high LFC cases within the set of supercells shown in Fig. 8, then increases in both WMAX and WAREA5 are apparent (not shown) as the hodograph radius increases, consistent with the trends for the other CAPE classes in that figure.

Alteration of the shear profile parameter has expected results, because a change to "n" (i.e., a change to the vertical distribution of shear) changes the mean wind vector. Intercomparison of the various panels in Figs. 5–6 shows that supercell motion differences between distributed and concentrated low-level shear profiles are 4–6 m s^{-1} in most cases, with the largest deviations occurring when shear profiles are concentrated. Supercells in concentrated shear also tend to have stronger updrafts and larger amounts of low-level vorticity than their distributed shear counterparts. This corroborates the findings of Droegemeier et al. (1993), who found stronger low-level mesocyclones resulted from increased SRH, or "when the largest shears are confined to the shallowest depths" (Adlerman and Droegemeier 2005). The amount of deviation from the hodograph is, to some degree, a function of the shear profile itself. Note that our findings do not imply that large deviant motions cannot exist in distributed shear environments. Lilly (1982) used a purely circular hodograph with radius of 20 m s^{-1} and distributed shear to simulate a rotating storm with motion near the center of the hodograph. A large hodograph radius or completely circular hodograph can compensate for distributed shear and lead to large deviant motions.

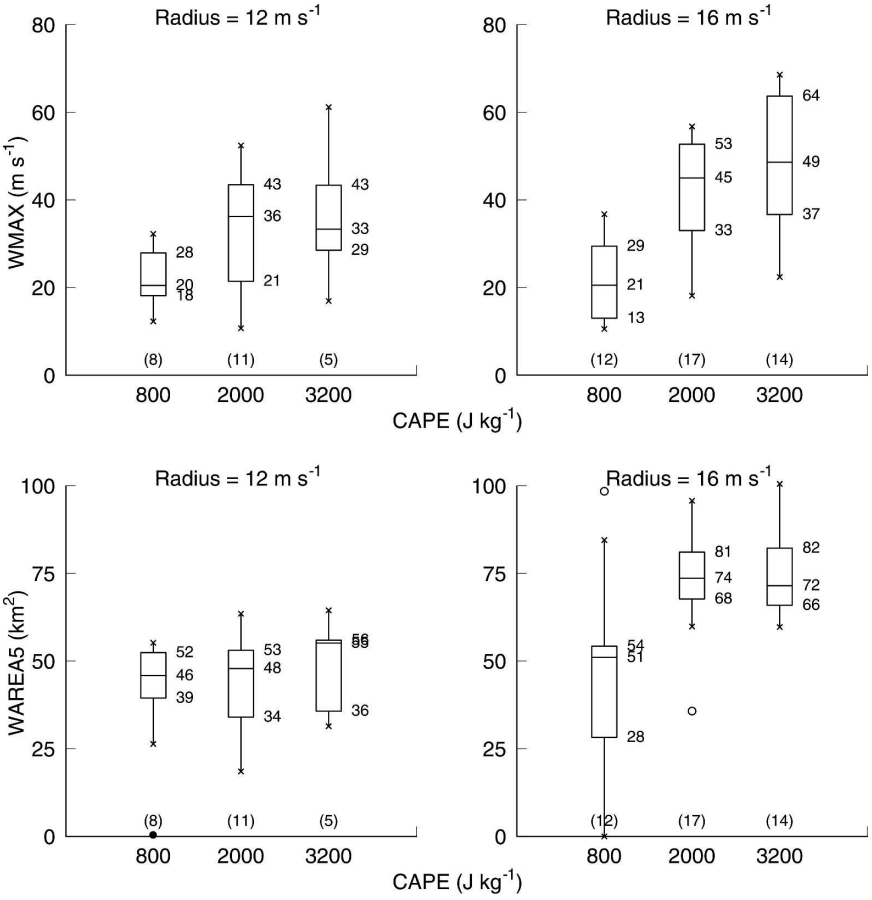

FIG. 8. Box-and-whiskers plots of WMAX and WAREA5 as a function of CAPE and hodograph radius. The box edges show the first (q1) and third (q3) quartiles, and the whiskers extend to the farthest data points that are still within a distance of 1.5 interquartile ranges from q1 and q3. Outliers beyond the whiskers are shown, in open circles up to a distance of three interquartile ranges beyond q3, and in closed circles beyond that. The number of simulations included is given in parentheses.

b. *Effects of buoyancy profile shape*

Thirty-six pairs of simulations of persistent storms with only the buoyancy profile shape varying are available for comparison.[7] No pairs exist at 800 CAPE; at this low CAPE value it is common for the distributed buoyancy member of the pair to fail to persist for the entire 2 h. In the 36 available pairs, concentrating buoyancy closer to the LFC has only marginal effects on deviate motion, increasing off-hodograph movement by an average of 1 m s^{-1} for supercells (1.7 m s^{-1} for nonsupercells). The supercell mean updrafts are only slightly more intense, increasing by about 5% (27% for nonsupercells) when the buoyancy profile is concentrated. This increase is smaller than anticipated because, unlike the simulations used in MW01, pairs in which only one member survived are not considered. In available pairs of supercells, however, some changes to storm evolution are noted in both groups. Increasing low-level buoyancy leads to increases in near-surface vorticity by 30%–50% at the lowest model level, strengthens the mean low-level cold pool temperature deficits by 30%–40%, and leads to an average 50% increase in the hail mixing ratio near the surface. It is not surprising that storm motion should be affected at least somewhat by these properties.

c. *Effects of LCL and LFC heights*

Supercell motion sensitivity to changes in mixed layer depth (i.e., LCL height; stars compared with filled

[7] Seventeen of the experiment pairs were composed of two supercells, and nineteen of two nonsupercells. No pairs composed of one supercell and one nonsupercell were included.

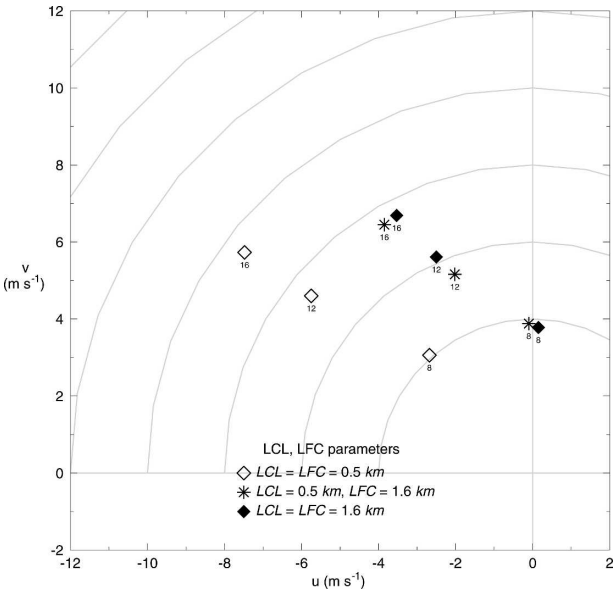

FIG. 9. The effects of LCL and LFC height on supercell motion as a function of hodograph radius. Each point is the average motion of all supercells with the given LCL and LFC heights. Subscripts denote the hodograph radius (R; m s^{-1}).

diamonds in Figs. 5 and 6) is generally below the 2 m s^{-1} threshold. This is somewhat surprising, because MC02 showed that mixed layer depth is an important regulator of storm outflow dominance. Raising the LCL from 0.5 to 1.6 km (while holding the LFC equal to 1.6 km) causes an average increase in ground-relative speed of only 0.3 m s^{-1} and increases deviation off the hodograph by only 0.4 m s^{-1}, both within the "noise" of our simulations. Updrafts are about 7% stronger, on average, when LCLs are high (average 42.6 m s^{-1} at high LCL, 39.8 m s^{-1} at low LCL). As in section 3b, this increase is smaller than that suggested by the results of MC02, primarily because we exclude here all potential comparison pairs for which one member, usually the low LCL member, fails to meet our updraft strength criteria. Although storm motions are not very sensitive to LCL variations, an increase in LFC height (while holding the LCL at 0.5 km) causes the motion vector to change significantly, by an average of 3.6 m s^{-1} (Fig. 9), essentially all in the direction of the deep layer (i.e., 0–10 km) shear vector (3.5 m s^{-1}). Because all our hodographs are approximately semicircles, this is analogous to an increase in the u component of the ground relative motion. This effect occurs at all hodograph radii and coincides with a significant increase in mean updraft velocity, rain and hail production, and the footprint area of the precipitation core.

When the LCL and LFC are both low (open diamonds in Figs. 5, 6, and 9), updrafts tend to be narrower and suffer more mixing and dilution of their buoyancy than when their LFCs are high (see MC02). Furthermore, condensate loading occurs over a deeper layer in the storm and restrains upward motion (Orville and Chen 1982). The low LCL storms also experience less subcloud evaporation of precipitation, because of the higher subcloud relative humidity. Their updrafts are thus less prone to outflow dominance and also deviate less from the mean wind than updrafts with a low LCL but a raised LFC. A raised LFC is beneficial for optimizing updraft overturning efficiency [the ratio of actual peak updraft speed to $(2\text{CAPE})^{0.5}$; MC02], allowing updrafts to be stronger and produce more precipitation. Updrafts in high LCL–high LFC environments (filled diamonds) produce larger cold pools owing to the increased depth of subsaturated air below cloud base and have less vorticity near the surface (i.e., at the lowest model level, 126 m AGL), but are otherwise statistically similar to the supercells in the low LCL–high LFC simulations, in terms of storm motion deviations.

d. Effects of cloud-base temperature

The temperature at cloud base is related to the liquid water–producing potential of a cloud (Cotton and Anthes 1989, 5–6), and is a proxy for PW. Large (warm) and small (cold) symbols in Figs. 5 and 6 denote the PW contents (cloud-base temperatures) in our experiments. All other parameters held equal, in every comparison of a supercell with high PW to low PW, a decrease in PW causes an increase in second-hour mean updraft velocity (see also MCK05), and in 91% (20 of 22) of the comparisons the low PW storm deviates farther off the hodograph (Fig. 10). The average change in vector motion in these 22 pairs (altering only PW) is 2.0 m s^{-1}.

e. Effects of bulk CAPE and its stratification

To study in more detail the effects of bulk CAPE on our simulated storms, a special set of 2000-CAPE, R = 12 m s^{-1} simulations was created that uses buoyancy and shear profile shapes identical to those already shared by the 800- and 3200-CAPE experiments (i.e., "m3n3"; see Figs. 1 and 2), while varying LCL and LFC height and cloud-base temperature. However, none of the 800-CAPE simulations having this profile shape parameter produced a supercell (or even a nonsupercell) that persisted through the entire simulation. Many of the low LCL–low LFC simulations at 2000 CAPE also struggled to persist, so broad conclusions based on CAPE variations are difficult. Of the (supercell *and* nonsupercell) storms that did survive, however, a trend toward increased off-hodograph deviation is noted as

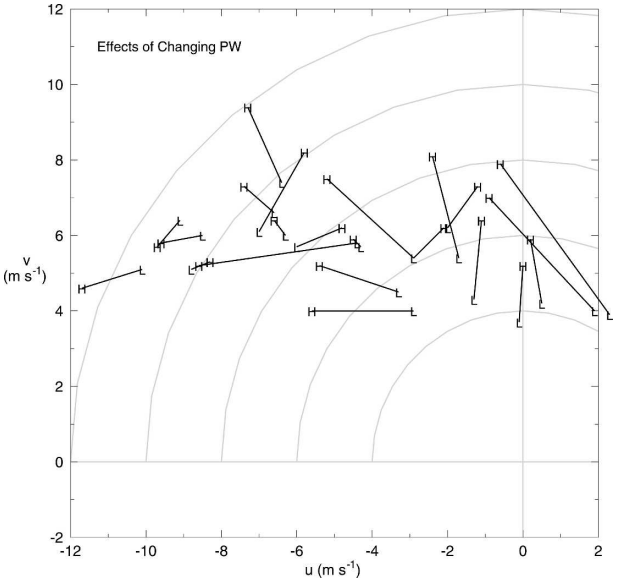

FIG. 10. The effects on supercell motion of changes in precipitable water. Simulation "pairs" with all parameters held constant other than PW are connected with lines. The "L" ("H") denotes a simulation with PW = 30 (60) mm.

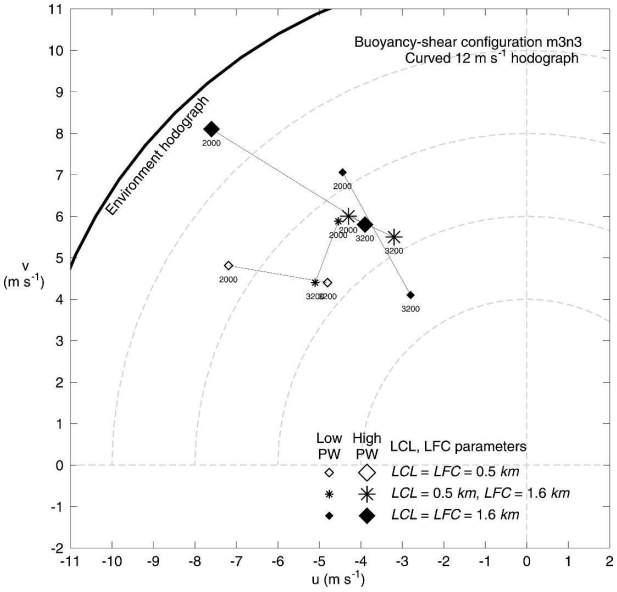

FIG. 11. Second-hour motions for individual experiments with buoyancy-shear configuration m3n3. Experiment groups with all parameters equal except for increasing CAPE (symbol subscript) are connected. The low LCL–LFC and low PW pair consists of supercells; the other eight storms are nonsupercells.

CAPE is increased from 2000 to 3200 J kg^{-1} (an average increase of 2.3 m s^{-1}; Fig. 11). The trend appears strongest when the LCL and LFC are both raised. Generally stronger updrafts with larger amounts of midlevel vertical vorticity (and thus a greater propensity for deviate motion) exist in persistent storms if the CAPE is increased as long as adequate shear is present. Larger and colder surface cold pools also accompany the increased-CAPE storms, so the increased deviate motion may be a combination of stronger rotating updrafts and enhanced propagation along the storm outflow. Exploration of additional bulk CAPE values may be beneficial in diagnosing this trend.

4. Discussion

a. General results

The magnitude of supercell deviate motion is dominated by the properties of the ambient shear profile, increasing when the hodograph radius is enlarged and when the low-level shear is increased. We find however that additional variations in motion occur as a result of changes to the ambient temperature and moisture profiles. Supercells generally deviate farther from the hodograph when the LFC is raised, when PW is decreased, and when buoyancy is concentrated close to the LFC. Increased CAPE increases the deviate motion of nonsupercells, but the impact on supercells is less obvious. These changes to the environmental thermodynamic sounding also frequently produce stronger updrafts that can increase the "updraft–shear interactions," which promote deviate motion (Rotunno and Klemp 1985). Our simulated supercells deviate farther off the hodograph than the nonsupercells (Fig. 7), but the sensitivities to other (thermodynamic) environmental changes are similar in both groups.

Generally speaking, the updraft–shear interactions that promote deviate motion are increased when the updraft is stronger. Updraft velocity is increased either when CAPE is larger (if shear is adequate), low-level buoyancy is increased and low-level lapse rates are maximized, when updrafts are burdened with less water and ice mass, or when the LFC is moderately elevated (discussed below). The vertical shear profile affects deviate motion by promoting vertical pressure gradients that allow storms to propagate rightward or leftward off the hodograph and away from the mean wind. In the supercell simulations, there is a strong correlation (r = 0.76) in the second hour between the midlevel pressure perturbations associated with the updraft and the magnitude of deviate motion. The correlation is even greater (r = 0.87) for simulated nonsupercell storms, although the amplitudes of the pressure and deviate motion variations are small.

Our results show that storms in low PW environments are more likely to deviate strongly from the mean wind (Fig. 10). The low PW environment, corre-

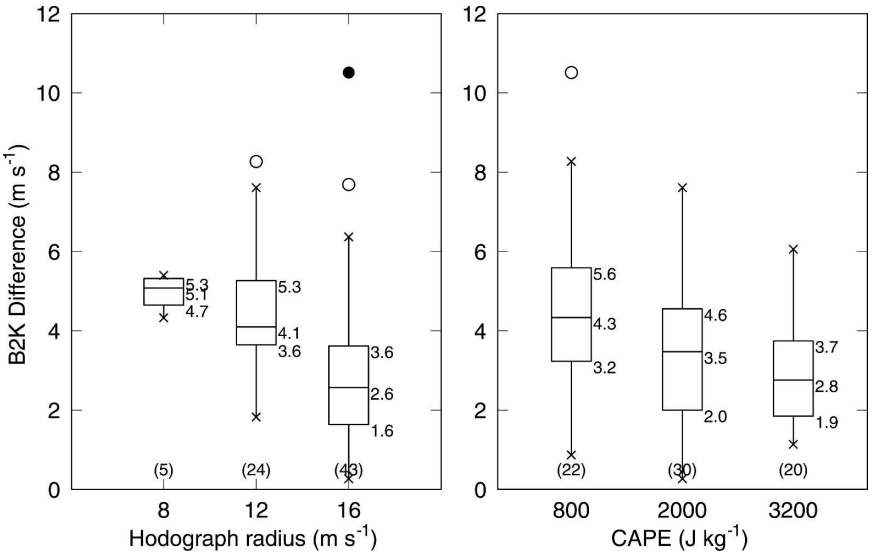

FIG. 12. Box-and-whiskers plots (same as in Fig. 8) of supercell B00 forecast differences as a function of hodograph radius and CAPE. Differences for hodograph radius are significant at the 90% confidence level; for CAPE, the differences are significant at 90% only for 800 vs 2000 CAPE.

sponding to a colder cloud base, represents a generally cooler environment. This increases the contribution to buoyant energy from the latent heat of fusion over a deeper layer of the atmosphere (the melting level is approximately 1.2 km lower in the cooler environments). Condensate loading is also usually reduced in the updraft when PW is small. Updraft overturning efficiencies are thus closer to unity and stronger updraft speeds are produced in the low PW cases (MCK05). In contrast, updrafts are usually weaker in the warmer, high PW environment; surface hail mixing ratios are also less as a result of increased melting. Some of the behavioral differences based on PW can be explained by considering reversible CAPE (e.g., MCK05), which includes the negative buoyancy effects of condensate loading. Thus, reversible CAPE will be substantially lower in the high PW simulations, even when pseudoadiabatic CAPE was specified to be equal for both high and low PW. In some cases, reversible CAPE may be superior to pseudoadiabatic CAPE in predicting updraft strength.

One of the most striking results is the impact of the LCL–LFC configuration on supercell propagation. While variations in LCL height at constant LFC have little effect on the motion, we find a linear correlation of 0.57 between LFC height and the component of supercell motion in the direction of the deep-layer shear (statistically significant at the 99% confidence level). Ramsay and Doswell's (2005) apparent finding that the surface–LCL layer is critical to supercell motion forecasts, when coupled with our results that indicate LFC height *is* related to storm motion, suggest that the appropriate mean wind layer may extend from the surface to some height that may be related to the LFC. Further study could relieve motion forecasting techniques from using "arbitrary" choices for the mean wind and shear-layer depths.

Although Ramsay and Doswell report "no statistically significant correlations" between errors associated with B00 and certain thermodynamic variables (CAPE, LCL height, LFC height, and equilibrium level height), we find that B00 most closely matches our simulated storm motions when the hodograph radius is large (Fig. 12a) and when CAPE is large (Fig. 12b). The mean B00 difference is also slightly smaller (3.3–4.1 m s^{-1}) for the low PW supercells compared with those in high PW. There are numerous reasons why a supercell motion forecast can be in error (e.g., Bunkers and Zeitler 2000), and the thermodynamic environment may play an additional part in explaining the magnitude of those errors.

b. Other considerations

While not studied herein, FTRH is one of the COMPASS basic input parameters and deserves some discussion. All simulations described here use high values (90%) of relative humidity above the moist subcloud layer. Simulated updrafts fail to persist when the relative humidity above the LFC is roughly 60% or less, with entrainment of dry air aloft the primary culprit

TABLE 5. Mean standard deviations of storm motions ($m\ s^{-1}$) for supercell storms as a function of CAPE and LCL/LFC configuration, and the average among all supercells as a function of CAPE.

	CAPE ($J\ kg^{-1}$)		
LCL/LFC	800	2000	3200
0.5/0.5 km	0.98	1.50	2.00
0.5/1.6 km	1.17	1.89	2.07
1.6/1.6 km	1.52	1.60	1.50
Avg	1.24	1.65	1.91

restricting updraft survival (McCaul and Cohen 2004). Questions about model diffusion parameterizations notwithstanding, this finding suggests that, in the real atmosphere, the environment must be preconditioned to some degree before a sustained updraft can exist. Preconditioning often takes the form of persistent low-level convergence, for example, near a dryline (Schaefer 1986) or in a region of positive moisture advection.

The simulations of Gilmore and Wicker (1998) showed that midtropospheric humidity can significantly affect simulated storm morphology and evolution, with attendant implications for storm motion estimates. In the cases with very dry midlevel layers, they found that, over time, the thunderstorm updraft and mesocyclones weakened, compared with storms simulated in higher-humidity environments. Gilmore and Wicker also found that the vertical placement of dry layers affected surface outflow and updraft maintenance. The exclusion of ice physics from their simulations may have affected their results. However, tests with our model (not shown) indicate that, even with ice physics, the basic findings of Gilmore and Wicker are confirmed. Work continues on the investigation of the impacts of variations in specified uniform FTRH on storms, but preliminary indications are that impacts on storm motion are not very large.

c. Temporal variability of storm motions

A general trend toward increasing temporal variability in storm motion with increasing CAPE is evident in our simulations (Table 5), with no apparent sensitivity to LCL or LFC height or PW content. No notable changes in temporal variability occur when the shape of the shear profile is changed. At intermediate and low CAPE values, the variability is also a function of the buoyancy profile shape (not shown). Consistent with the sensitivity of deviate motions to CAPE, the strongest of the low CAPE storms exhibit the steadiest updrafts and motions. Although CAPE strongly influences the general amount of storm motion variability, increased low-level lapse rates can promote more pulselike updrafts that can also produce more variable storm motions. It should be noted that the variability shown in Table 5 is close to the mean variability among all supercells ($1.6\ m\ s^{-1}$; section 2). The Student's *t* test confirms that the difference in variability between 800 and 2000 CAPE is statistically significant (at the 99% confidence level), but that the difference between 2000- and 3200-CAPE supercells is not (even at the 90% confidence level).

Variability in storm motion can be caused by a trend (acceleration) or by oscillation about a mean value. In Table 6, we show second-hour motions and variances for three simulations having different values of CAPE, holding all other parameters constant (e.g., concentrated buoyancy and shear, low LCL, low LFC, and cold cloud-base temperature). Variance from the mean is expressed as the sum of the squares of the individual (5 min) motion differences from the second-hour mean. A "trend mean," calculated as the average of the 60- and 120-min motions, can also be used to calculate variance; the resulting values represent the variability from the storm motion trend. The variance from the trend itself (the line connecting the motions at 60 and 120 min) is a measure of the variance due to oscillations in storm motion. For the v component of motion, the variations caused by oscillations overwhelm variations caused by trends; the oscillatory variations are also larger (but not by as much) for the u component of motion. In all cases, both oscillatory and trend variances increase with increasing CAPE.

Investigation of selected time series plots associated

TABLE 6. Mean second-hour motions and different calculations of storm motion variance (discussed in the text) for three particular simulations with concentrated buoyancy, concentrated shear, a low LCL and LFC, and low PW. Motions are given in $m\ s^{-1}$ and variances in $m^2\ s^{-2}$.

	Mean motions in the second hour		Variance from mean (total variance)		Variance from trend mean (variance due to trend)		Variance from trend (variance due to oscillation)	
CAPE ($J\ kg^{-1}$)	u	v	u	v	u	v	u	v
800	−2.9	4.0	22.8	10.5	22.0	3.5	23.4	29.9
2000	−3.5	4.8	43.7	19.4	29.9	7.0	29.7	45.4
3200	−5.1	4.8	100.7	78.7	30.7	7.9	89.4	102.1

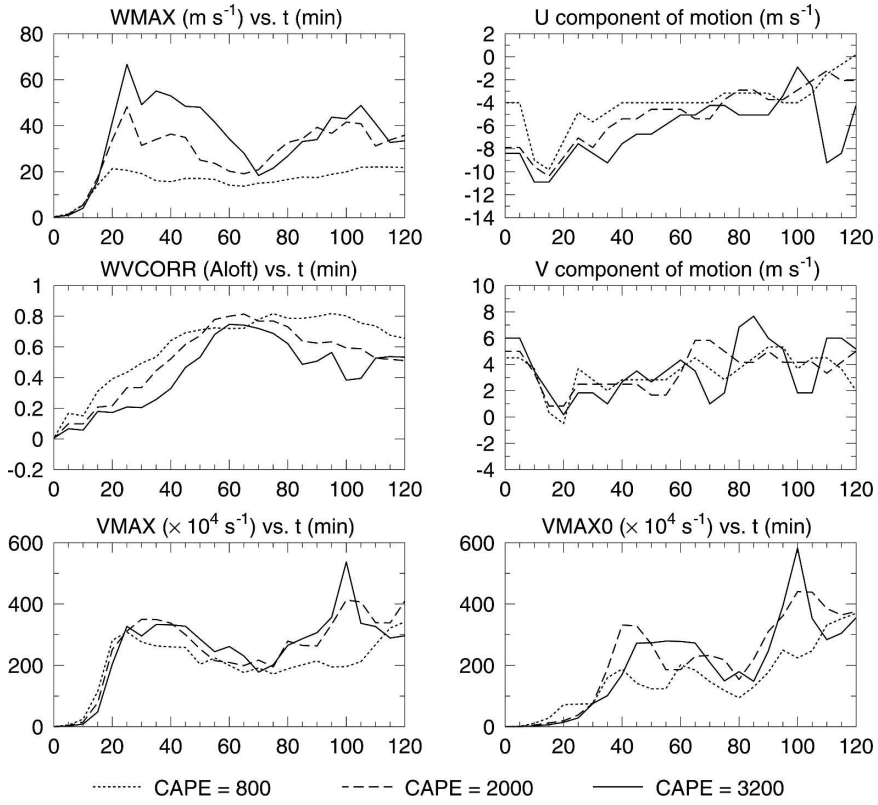

FIG. 13. Time series plots for three particular simulations with concentrated buoyancy, concentrated shear, a low LCL and LFC, and low PW: (a) maximum updraft velocity, (b) updraft–vorticity correlation, (c) maximum vorticity aloft, (d) ground-relative u motion, (e) ground-relative v motion, and (f) maximum vorticity at the lowest model level (126 m AGL).

with the three cases (Fig. 13) show that temporal changes in storm morphology become increasingly complex as CAPE is increased. The effects of initiation and an initial split can be seen in the first 30 min of each simulation. After the first 30 min, the updraft in the low (800) CAPE simulation remains at approximately 20 m s^{-1}. Although there are small variations in storm motion components during the simulation, the high updraft-vorticity correlation (WVCORR) and updraft constancy indicate a nearly steady-state circulation. At intermediate CAPE, somewhat greater-magnitude oscillations in motion exist in both u and v components, and the updraft velocity exhibits a large (20 m s^{-1}) cycle during the second hour. Vorticity also increases rapidly between 80 and 100 min, remaining high through the end of the simulation. At high CAPE, the most complicated mature storm evolution exists, with two large oscillations evident in the v component of motion. The first occurs during the 65–75-min interval, and coincides with a decrease in updraft velocity; subjective analysis of the simulation output confirms that a storm split occurs during this time. The second large-amplitude oscillation occurs during 100–110 min of simulation time and is related to the sharp decreases in vorticity aloft (VMAX) and at the model level near the surface (VMAX0), immediately after the two parameters peak. This is consistent with an occlusion of the updraft and mesocyclone (e.g., as in Adlerman et al. 1999). In general, much of the enhanced temporal variability in storm motions at large CAPE appears to derive from an increased susceptibility to storm splits and mesocyclone structural cycling in that part of the parameter space.

5. Summary and future work

The motion of a thunderstorm is closely related to the characteristics of the storm's ambient environment. We have used a cloud model containing ice physics to examine the variations in storm propagation as a function of vertical variations in temperature, humidity, and wind. While storm deviate motion is dominated by the ambient shear profile, the motion is also influenced to some degree by the thermodynamic profile. Specific properties of the thermodynamic profile can lead to stronger updrafts and enhance familiar updraft–shear

interactions, which, in an environment with vertical wind shear, are associated with vertical pressure gradients on the flanks of the updrafts that can cause propagation off the hodograph.

The present results establish the relative importance of the basic thermodynamic parameters as potential influences on storm motion. Traditional methods of forecasting storm motion based solely on hodograph characteristics (e.g., B00) could thus benefit from revision to account for the influence of these other thermodynamic aspects of the storm environment. These revisions, for example, might take the form of modification to existing constants, new choices of layer depths used, or the addition of new terms to the forecast equation. The sensitivity of storm motion temporal variability must also be considered, as the present findings show increased variability of storm motion in higher CAPE environments. The results also call attention to the importance of using a priori techniques to anticipate convective mode (i.e., supercell versus nonsupercell), since the magnitude of deviate motion is found to be dependent on this classification.

As in the real atmosphere, the effects described here are inherently nonlinear. If CAPE is small, a high PW content can suppress persistent convection altogether, especially if low-level lapse rates are weak (i.e., the buoyancy profile is "distributed"). When CAPE increases, cold pools and surface outflows become larger and stronger and increase the likelihood of outflow dominance and multicellular behavior, especially if LCLs are high and shear inadequate. The narrow updrafts generated in low CAPE–low LFC regimes often fail to persist through the entire 2 h of the simulations, except when low-level buoyancy is strong and PW is small. The present results suggest that storms in environments with strong shear and steep low-level lapse rates, a low LCL and high LFC, and relatively cool cloud-base temperatures produce updrafts with the greatest deviate motions. The variability of the updrafts and deviate motions was found to be greater when CAPE was large; our steadiest supercells occur when CAPE = 800 J kg^{-1}.

Opportunities exist for continued analysis of the present numerical simulation set to further examine storm motion and morphology. Statistical analysis of thermodynamic parameter sensitivities to devise refinements to the B00 method is a desirable next step. It is possible that the MAE of the B00 method could be reduced by including these refinements. Additional case study simulations, as well as studies of how often the real atmosphere "visits" the different parts of our parameter space (Nair et al. 2002), should be considered. The changes in storm motion that are associated with variations in the LCL and LFC heights should be explored in greater detail. Additional hodograph shapes (e.g., Weisman and Rotunno 2000; Adlerman and Droegemeier 2005) may also yield further variations in storm morphology and evolution. The manner in which storms are initiated can affect storm mode in the real atmosphere (e.g., in response to frontally forced circulations or terrain); it is expected that a similar sensitivity would also exist with numerically modeled convection. The variability arising from different microphysical specifications and their resulting precipitation distributions (Cohen and McCaul 2006; also noted in section 2) should also be considered. Finally, the present simulation length presents a relatively short time window to fully diagnose storm motion trends and updraft occlusion cycles; extension of some simulations beyond 2 h may provide more insight into this aspect of storm motion variability.

Acknowledgments. This research is a part of the Convection Morphology Parameter Space Study (COMPASS), which is supported by Grant ATM-0126408 from the National Science Foundation, under the supervision of Dr. Stephan Nelson. Publication support was provided by Grant 745245 from the National Oceanic and Atmospheric Administration. The authors are grateful for the reviews and constructive criticisms of Dr. Matthew Bunkers and two additional anonymous reviewers; their comments significantly improved this manuscript. The COMPASS numerical simulations were conducted on the Matrix linux cluster at the University of Alabama in Huntsville (UAH). We are grateful to Dr. Don Perkey for his assistance with various aspects of the COMPASS project. We also acknowledge programming support from Jayanthi Srikishen of USRA in Huntsville, and computer system support from Scott Podgorny, UAH, throughout this project. (For additional information on the COMPASS study, see our Web site online at http://space.hsv.usra.edu/COMPASS.)

APPENDIX

Verification of Model-Predicted Storm Motions

To establish that storm motions produced by our simulations are reasonable compared to storms that are observed in the real atmosphere, a series of case study simulations was conducted. Each case selected is believed to represent an environment where the effects of any preexisting mesoscale boundaries or forcing are negligible, thus making our "thermal bubble" approach to initiation appropriate for reproducing a good approximation to the actual storm. The cases represent a wide array of atmospheric regimes. We present one

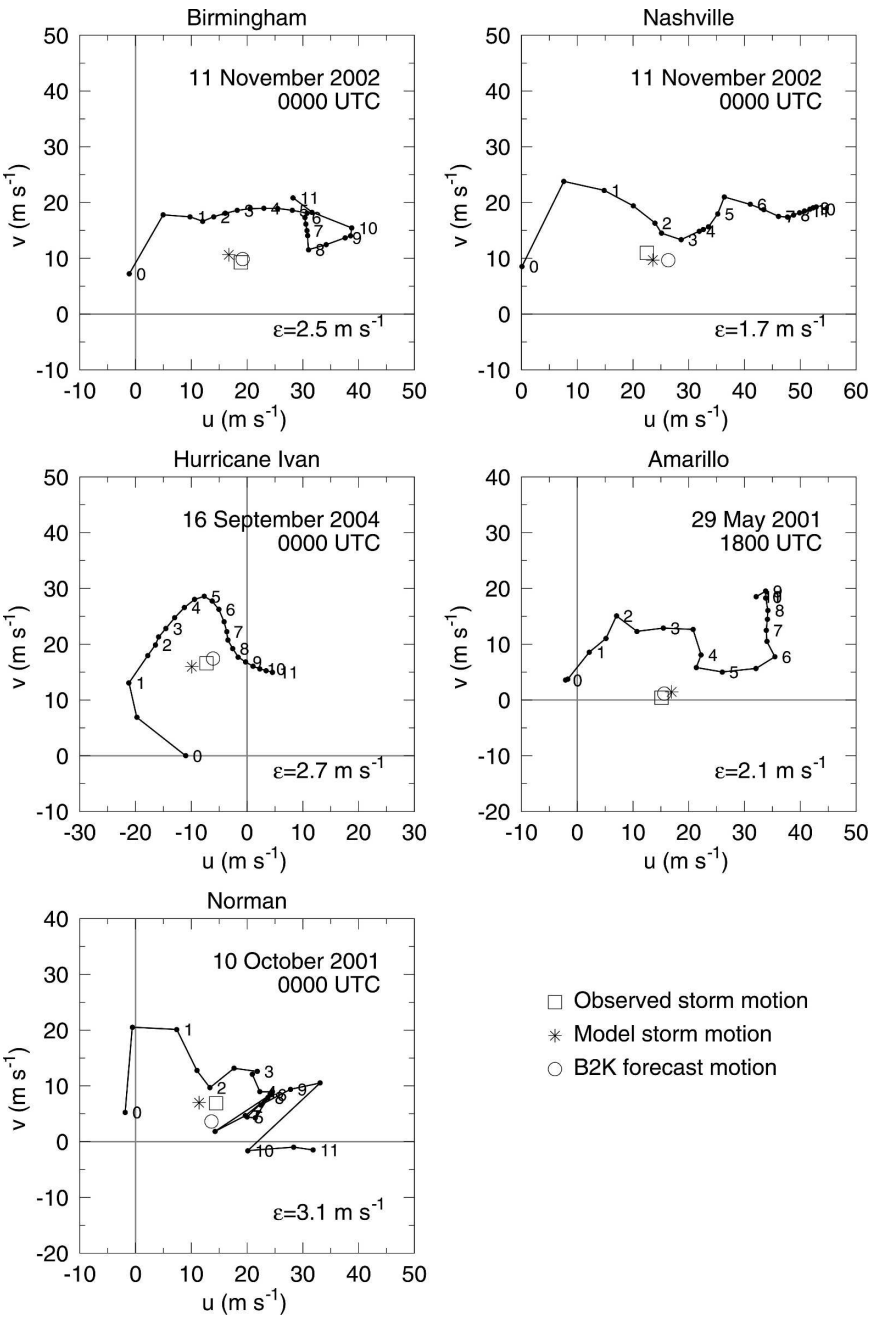

FIG. A1. Hodographs for the five case studies discussed in the text, with symbols every 0.5 km and labels every 1 km. The magnitude of the vector difference between the model and observed storm motion is given as ε.

tropical case (supercells associated with land-falling Hurricane Ivan on 16 September 2004), two southern plains cases (storms near Amarillo, Texas, on 29 May 2001 and west of Oklahoma City, Oklahoma, on 9 October 2001), and two cases with rapidly moving supercells in the Southeast (near Birmingham, Alabama, and near Nashville, Tennessee, on 10 November 2002). Input hodographs, and observed and simulated storm motions, are presented in Fig. A1.

For the two 10 November 2002 cases, the wind profiles from rawinsondes launched by the National Weather Service offices in Birmingham (BMX) and in Nashville (BNA) at 0000 UTC 11 November 2002 were used. At BNA, wind data above 500 mb were missing

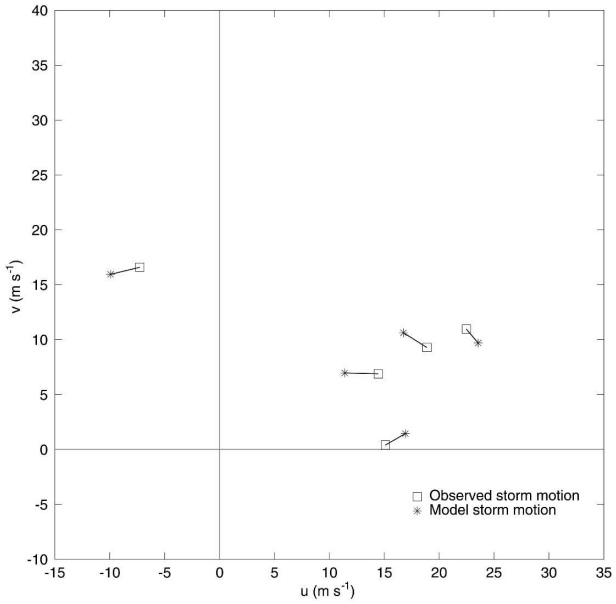

FIG. A2. Plot of the differences between radar-derived and model-simulated storm motions for the five case studies presented in Fig. A1.

and replaced with data from the 0000 UTC 11 November 2002 ETA 0-h forecast at the nearest grid point. The winds aloft at BNA were considerably stronger than those at BMX. Based on inspection of surface observations, the unmodified thermodynamic profile from BMX was used in both cases.

We began our simulation of the 29 May 2001 case with the 1800 UTC sounding from Amarillo (AMA), but with an additional 250 m of moist air at the bottom because observed storms were east of the Caprock Escarpment in the Texas panhandle (see, e.g., Doswell 1982). In addition, the upper-level winds were veered slightly (10° in the 700–500-mb layer and 20° above) to account for the veering associated with an advancing jet streak as evident in the 0000 UTC 30 May AMA winds. The mid- and upper-level winds for the 9 October 2001 case in western Oklahoma were similarly veered, based on starting soundings from Norman, Oklahoma (OUN), and AMA at 00 UTC 10 October 2001. The 9 October 2001 thermodynamic profile was adjusted at low levels to represent surface conditions near where storm initiation occurred.

In Hurricane Ivan, tornadic supercells occurred in the Florida panhandle, and were the target of our simulation. For the simulation of the Hurricane Ivan environment, the thermodynamic profile of the Tallahassee, Florida (TLH), sounding at 0000 UTC 16 September 2004 was used as a starting point. Because of the existence of strong gradients in winds near Ivan, the wind profile used was the 0-h forecast from the 0000 UTC North American Mesoscale model run at a grid point just west of TLH. The surface observation at Panama City, Florida, was blended with these data to create the input profile. The "observed" storm motion for 0000 UTC conditions was calculated by averaging observed storm motions from a cluster of storms offshore, approximately 60 miles south of TLH, and other storms observed the same distance north of TLH. In all cases, observed storm motions were determined using archived data from the National Weather Service Weather Surveillance Radar-1988 Doppler (WSR-88D) network.

In every case, our simulations produce good agreement with the motion of the observed storms, with speed errors (denoted as ε in Fig. A1) of about 2–3 m s^{-1}. These errors are comparable to the temporal variability of the simulated storm motions for high CAPE cases discussed in this paper. They are also comparable to the errors that occur when using the B00 method (mean model error 2.4 versus 2.1 m s^{-1} for B00). The errors show little bias toward the location of storm motion on the hodograph (Fig. A2). These results give us confidence that our model is suitable for examining the motions of simulated convective storms in a wide variety of environmental conditions.

REFERENCES

Adlerman, E. J., and K. K. Droegemeier, 2005: The dependence of numerically simulated cyclic mesocyclogenesis upon environmental vertical wind shear. *Mon. Wea. Rev.,* **133,** 3595–3623.

——, ——, and R. P. Davies-Jones, 1999: Numerical simulation of cyclic mesocyclogenesis. *J. Atmos. Sci.,* **56,** 2045–2069.

Akaeda, K., J. Reisner, and D. Parsons, 1995: The role of mesoscale and topographically induced circulations in initiating a flash flood observed during the TAMEX project. *Mon. Wea. Rev.,* **123,** 1720–1739.

Bolton, D., 1980: The computation of equivalent potential temperature. *Mon. Wea. Rev.,* **108,** 1046–1053.

Brooks, H. B., 1946: A summary of some radar thunderstorm observations. *Bull. Amer. Meteor. Soc.,* **27,** 557–563.

Brooks, H. E., and R. B. Wilhelmson, 1993: Helicity and updraft intensity in numerically modeled supercells. *J. Atmos. Sci.,* **50,** 1824–1833.

——, C. A. Doswell III, and J. Cooper, 1994: On the environments of tornadic and nontornadic mesocyclones. *Wea. Forecasting,* **9,** 606–618.

Browning, K. A., 1962: Cellular structure of convective storms. *Meteor. Mag.,* **91,** 341–350.

——, 1964: Airflow and precipitation trajectories within severe local storms which travel to the right of the winds. *J. Atmos. Sci.,* **21,** 634–639.

Bunkers, M. J., and J. W. Zeitler, 2000: On the nature of highly deviant supercell motion. Preprints, *20th Conf. on Severe Local Storms,* Orlando, FL, Amer. Meteor. Soc., 236–239.

——, B. A. Klimowski, J. W. Zeitler, R. L. Thompson, and M. L.

Weisman, 2000: Predicting supercell motion using a new hodograph technique. *Wea. Forecasting,* **15,** 61–79.

——, J. S. Johnson, L. J. Czepyha, J. M. Grzywacz, B. A. Klimowski, and M. R. Hjelmfelt, 2006: An observational examination of long-lived supercells. Part II: Environmental conditions and forecasting. *Wea. Forecasting,* **21,** 689–714.

Byers, H. R., and R. R. Braham, 1949: *The Thunderstorm*. U.S. Government Printing Office, 287 pp.

Cohen, C., and E. W. McCaul Jr., 2006: The sensitivity of simulated convective storms to variations in prescribed single-moment microphysics parameters that describe particle distributions, sizes, and numbers. *Mon. Wea. Rev.,* **134,** 2547–2565.

Colquhoun, J. R., 1980: A method of estimating the velocity of a severe thunderstorm using the vertical wind profile in the storm's environment. Preprints, *Eighth Conf. on Weather Forecasting and Analysis,* Denver, CO, Amer. Meteor. Soc., 316–323.

Corfidi, S. F., 2003: Cold pools and MCS propagation: Forecasting the motion of downwind-developing MCSs. *Wea. Forecasting,* **18,** 997–1017.

Cotton, W. R., and R. A. Anthes, 1989: *Storm and Cloud Dynamics*. Academic Press, 883 pp.

Davies, J., and R. Johns, 1993: Some wind and instability parameters associated with strong and violent tornadoes. 1. Wind shear and helicity. *The Tornado: Its Structure, Dynamics, Prediction, and Hazards, Geophys. Monogr.,* Vol. 79, Amer. Geophys. Union, 573–582.

Davies-Jones, R. P., 1984: Streamwise vorticity: The origin of updraft rotation in supercell storms. *J. Atmos. Sci.,* **41,** 2991–3006.

——, 2002: Linear and nonlinear propagation of supercell storms. *J. Atmos. Sci.,* **59,** 3178–3205.

Doswell, C. A., III, 1982: The operational meteorology of convective weather. Vol. I: Operational mesoanalysis. U.S. Dept. of Commerce/NOAA Tech. Memo. NWS NSSFC-5, 158 pp.

Droegemeier, K. K., S. M. Lazarus, and R. Davies-Jones, 1993: The influence of helicity on numerically simulated convective storms. *Mon. Wea. Rev.,* **121,** 2005–2029.

Foote, G. B., 1985: Aspects of cumulonimbus classification relevant to the hail problem. *J. Rech. Atmos.,* **19,** 61–74.

Gilmore, M., and L. J. Wicker, 1998: The influence of midtropospheric dryness on supercell morphology and evolution. *Mon. Wea. Rev.,* **126,** 943–958.

Klemp, J. B., and R. B. Wilhelmson, 1978: The simulation of three-dimensional convective storm dynamics. *J. Atmos. Sci.,* **35,** 1070–1096.

Landel, G., J. A. Smith, M. L. Baeck, M. Steiner, and F. L. Ogden, 1999: Radar studies of heavy convective rainfall in mountainous terrain. *J. Geophys. Res.,* **104,** 31 451–31 466.

Lemon, L. R., 1976: The flanking line, a severe thunderstorm intensification source. *J. Atmos. Sci.,* **33,** 686–694.

Lilly, D. K., 1962: On the numerical simulation of buoyant convection. *Tellus,* **14,** 148–172.

——, 1982: The development and maintenance of rotation in convective storms. *Intense Atmospheric Vortices,* L. Bengtsson and J. Lighthill, Eds., Springer-Verlag, 149–160.

Maddox, R. A., 1976: An evaluation of tornado proximity wind and stability data. *Mon. Wea. Rev.,* **104,** 133–142.

Markowski, P. M., E. N. Rasmussen, and J. M. Straka, 1998: The occurrence of tornadoes in supercells interacting with boundaries during VORTEX-95. *Wea. Forecasting,* **13,** 852–859.

Marroquin, A., and D. J. Raymond, 1982: A linearized convective overturning model for the prediction of thunderstorm movement. *J. Atmos. Sci.,* **39,** 146–151.

Marwitz, J. D., 1972a: The structure and motion of severe hailstorms. Part I: Supercell storms. *J. Appl. Meteor.,* **11,** 166–179.

——, 1972b: The structure and motion of severe hailstorms. Part II: Multicell storms. *J. Appl. Meteor.,* **11,** 180–188.

McCaul, E. W., Jr., 1991: Buoyancy and shear characteristics of hurricane-tornado environments. *Mon. Wea. Rev.,* **119,** 1954–1978.

——, and M. L. Weisman, 2001: The sensitivity of simulated supercell structure and intensity to variations in the shapes of environmental buoyancy and shear profiles. *Mon. Wea. Rev.,* **129,** 664–687.

——, and C. Cohen, 2002: The impact on simulated storm structure and intensity of variations in the mixed layer and moist layer depths. *Mon. Wea. Rev.,* **130,** 1722–1748.

——, and ——, 2004: The initiation, longevity and morphology of simulated convective storms as a function of free-tropopheric relative humidity. Preprints, *22d Conf. on Severe Local Storms,* Hyannis, MA, Amer. Meteor. Soc., CD-ROM, 8A.5.

——, ——, and C. Kirkpatrick, 2005: The sensitivity of simulated storm structure, intensity, and precipitation efficiency to environmental temperature. *Mon. Wea. Rev.,* **133,** 3015–3037.

Nair, U. S., E. W. McCaul Jr., and R. M. Welch, 2002: Climatology of environmental parameters that influence severe storm intensity and morphology. Preprints, *16th Conf. on Hydrology,* Orlando, FL, Amer. Meteor. Soc., CD-ROM, 2.4.

Newton, C. W., and H. R. Newton, 1959: Dynamical interactions between large convective clouds and environment with vertical shear. *J. Meteor.,* **16,** 483–496.

Orville, H. D., and J.-M. Chen, 1982: Effects of cloud seeding, latent heat of fusion, and condensate loading on cloud dynamics and precipitation evolution: A numerical study. *J. Atmos. Sci.,* **39,** 2807–2827.

Pielke, R. A., and Coauthors, 1992: A comprehensive meteorological modeling system—RAMS. *Meteor. Atmos. Phys.,* **9,** 69–91.

Ramsay, H. A., and C. A. Doswell III, 2005: A sensitivity study of hodograph-based methods for estimating supercell motion. *Wea. Forecasting,* **20,** 954–970.

Rasmussen, E. N., and D. O. Blanchard, 1998: A baseline climatology of sounding-derived supercell and tornado forecasting parameters. *Wea. Forecasting,* **13,** 1148–1164.

Rotunno, R., and J. B. Klemp, 1982: The influence of the shear-induced pressure gradient on thunderstorm motion. *Mon. Wea. Rev.,* **110,** 136–151.

——, and ——, 1985: On the rotation and propagation of simulated supercell thunderstorms. *J. Atmos. Sci.,* **42,** 271–292.

Schaefer, J. T., 1986: The dryline. *Mesoscale Meteorology and Forecasting,* P. S. Ray, Ed., Amer. Meteor. Soc., 549–572.

Shapiro, A., P. Robinson, J. Wurman, and J. Gao, 2003: Single-Doppler velocity retrieval with rapid-scan radar data. *J. Atmos. Oceanic Technol.,* **20,** 1758–1775.

Smagorinsky, J., 1963: General circulation experiments with the primitive equations. Part I: The basic experiment. *Mon. Wea. Rev.,* **91,** 99–164.

Tripoli, G. J., and W. R. Cotton, 1982: The Colorado State University three-dimensional cloud/mesoscale model–1982. Part I: General theoretical framework and sensitivity experiments. *J. Rech. Atmos.,* **16,** 185–219.

van den Heever, S., and W. R. Cotton, 2004: The impact of hail

size on simulated supercell storms. *J. Atmos. Sci.,* **61,** 1596–1609.

Walko, R. L., W. R. Cotton, M. P. Meyers, and J. Y. Harrington, 1995: New RAMS cloud microphysics parameterization. Part I: The single-moment scheme. *Atmos. Res.,* **38,** 29–62.

Weaver, J. F., and S. P. Nelson, 1982: Multiscale aspects of thunderstorm gust fronts and their effects on subsequent storm development. *Mon. Wea. Rev.,* **110,** 707–718.

Weckwerth, T. M., and D. B. Parsons, 2006: A review of convection initiation and motivation for IHOP_2002. *Mon. Wea. Rev.,* **134,** 5–22.

Weisman, M. L., and J. B. Klemp, 1982: The dependence of numerically simulated convective storms on vertical wind shear and buoyancy. *Mon. Wea. Rev.,* **110,** 504–520.

——, and ——, 1984: The structure and classification of numerically simulated convective storms in directionally varying shears. *Mon. Wea. Rev.,* **112,** 2479–2498.

——, and R. Rotunno, 2000: The use of vertical wind shear versus helicity in interpreting supercell dynamics. *J. Atmos. Sci.,* **57,** 1452–1472.

Wilhelmson, R. B., and J. B. Klemp, 1978: A numerical study of storm splitting that leads to long-lived storms. *J. Atmos. Sci.,* **35,** 1974–1986.

Wilson, J. W., and R. D. Roberts, 2006: Summary of convective storm initiation and evolution during IHOP: Observational and modeling perspective. *Mon. Wea. Rev.,* **134,** 23–47.

Zeitler, J. W., and M. J. Bunkers, 2005: Operational forecasting of supercell motion: Review and case studies using multiple datasets. *Natl. Wea. Dig.,* **29,** 81–97.